Design principles for selective self-assembly of active networks

Simon L. Freedman,[1] Glen M. Hocky,[2] Shiladitya Banerjee,[3,*] and Aaron R. Dinner[2,†]

[1] *Department of Physics, University of Chicago*
[2] *Department of Chemistry and James Franck Institute, University of Chicago*
[3] *Department of Physics and Astronomy, University College London*

Living cells dynamically modulate the local morphologies of their actin cytoskeletons to perform biological functions, including force transduction, intracellular transport, and cell division. A major challenge is to understand how diverse structures of the actin cytoskeleton are assembled from a limited set of molecular building blocks. Here we study the spontaneous self-assembly of a minimal model of cytoskeletal materials, consisting of semiflexible actin filaments, crosslinkers, and molecular motors. Using coarse-grained simulations, we demonstrate that by changing concentrations and kinetics of crosslinkers and motors we can generate three distinct structural phases of actomyosin assemblies: bundled, polarity-sorted, and contracted. We introduce new metrics to distinguish these structural phases and demonstrate their functional roles. We find that the binding kinetics of motors and crosslinkers can be tuned to optimize contractile force generation, motor transport, and mechanical response. By quantitatively characterizing the relationships between modes of cytoskeletal self-assembly, the resulting structures, and their functional consequences, our work suggests new principles for the design of active materials.

Mechanical functions of living cells are determined by dynamic restructuring of the actin cytoskeleton, a highly conserved cellular machinery composed of filamentous actin (F-actin), myosin molecular motors, and crosslinking proteins [1]. An enormous variety of F-actin binding proteins exist, with a wide range of physico-chemical properties [2] that can combine with F-actin to assemble function-specific, cellular structures. Spatiotemporal control over these structures is essential for coordinated force generation during cell migration [3, 4], cell adhesion [5], cytokinesis [6], and intracellular transport [7, 8]. A quantitative understanding of how diverse cytoskeletal structures are assembled from a limited set of molecular building blocks presents an outstanding challenge at the interface of soft matter physics and cell biology.

Given the many interconnected molecular processes within cells, it is experimentally difficult to controllably study how variations in molecular-scale properties affect emergent actin network structures and function. To this end, *in vitro* biochemical studies have enabled major inroads to be made into uncovering how biochemical compositions and relative amounts of actin filaments and molecular motors determine network architectures and mechanical properties [9–17]. Additionally, it has been shown how the mechanical response of actin networks can be tuned by varying the types and amounts of crosslinkers involved [18–23].

Simulations complement experiments and theories [24–26] by allowing both precise control of the physical properties of constituents and examination of microscopic mechanisms. These features have enabled simulations to provide insights into contractility [14, 17, 27–29], viscoelastic properties [30, 31], transport [32], and structural rearrangements [33, 34]. While the structural phase diagram of filaments with passive crosslinkers has been mapped and shown to exhibit homogeneous isotropic gel, bundled, clustered, and lamellar phases [33], to the best of our knowledge, a corresponding study of active materials has not been performed previously. It remains to determine the network structures accessible to mixtures of filaments, crosslinkers, and motors, the conditions under which they are formed, and their relations to functions.

In this Letter, we map the non-equilibrium structural phases of cytoskeletal networks consisting of F-actin, crosslinkers, and myosin motors. We observe homogeneous, bundled, contracted, and polarity-sorted actin networks and characterize the parameters that control their assembly. In doing so, we introduce order parameters that can classify the extent to which networks contract into dense aggregates, sort F-actin by polarity, or bundle filaments into force propagating networks. Using these metrics, we demonstrate how actin networks can be selectively optimized for specific mechanical functionalities, by systematic variations in network composition, filament length, and kinetic properties of actin binding proteins.

Coarse-grained model. To study the spontaneous self-assembly of cytoskeletal structures at experimentally relevant length and time scales (microns and minutes), we use AFINES, a simulation framework we recently developed [20]. In brief, actin filaments are modeled as polar worm-like chains (represented by beads connected by springs) with defined barbed and pointed ends (Fig. 1); crosslinkers are modeled as linear springs with ends (heads) that can stochastically bind and unbind from F-actin via a kinetic Monte Carlo procedure that preserves detailed balance; molecular motors are modeled as active crosslinkers such that once bound, they walk toward the barbed end of F-actin at a load-dependent speed. We use Brownian dynamics to evolve the positions of constituents in 2D. Restriction to 2D is consistent with the fact that *in vitro* reconstitutions of actomyosin

* shiladitya.banerjee@ucl.ac.uk
† dinner@uchicago.edu

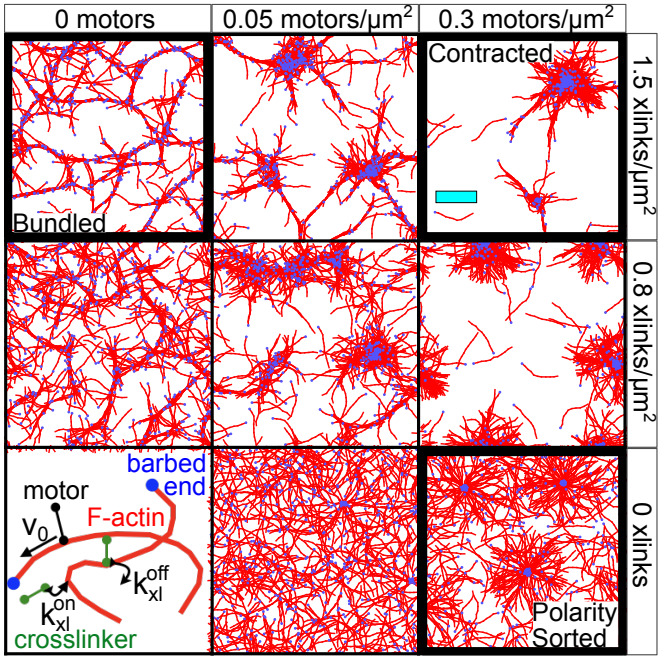

FIG. 1. Network structures. (Lower left) Schematic of the model [20] with F-actin in red, crosslinkers in green, and motors in black. Bound motors walk towards F-actin barbed ends in blue. (Remaining panels) Network structures at 400 s for indicated motor and crosslinker densities. These include a bundled network (upper left) formed by filaments and crosslinkers, a polarity-sorted network (lower right) formed by filaments and motors, and a contracted network (upper right) formed from filaments, crosslinkers, and motors. For clarity, only the actin filaments are shown; the motors and crosslinkers are shown in Fig. S1. Cyan scale bar represents 10 μm.

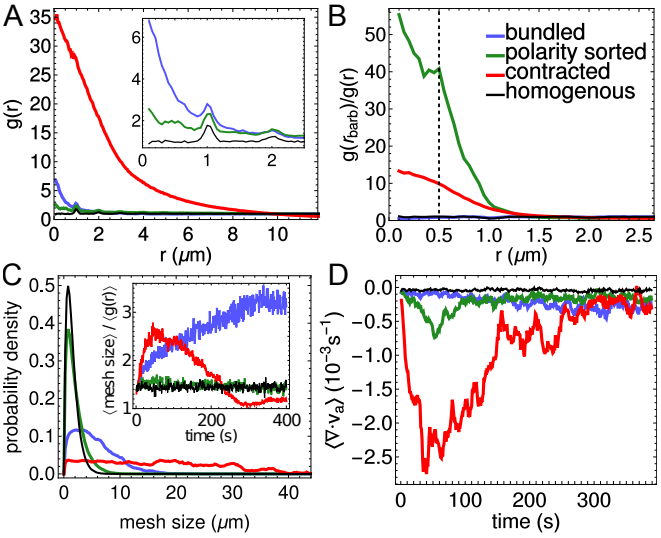

FIG. 2. Order parameters for characterizing network structures. Bundled, polarity-sorted, and contracted cases correspond to the conditions highlighted in Fig. 1; the homogeneous case has no motors or crosslinkers. (A) Radial distribution function of actin, $g(r)$, shows that the contracted system is substantially more aggregated than the other three cases. (B) Radial distribution function of F-actin barbed ends, normalized by $g(r)$, showing substantial barbed end aggregation in polarity-sorted networks; the dashed line marks the motor rest length, 0.5 μm. (C) Mesh size distribution, showing actin rearrangment for bundled and contracted networks. The inset shows the evolution of the average mesh size, normalized by $\langle g(r)\rangle$, distinguishing the bundled system. (D) Spatially averaged divergence (Section S3), distinguishing the contracted system. All averages are over the final 50 s of 5 simulations of 400 s.

networks are nearly flat [12, 17, 21]. To enable rearrangement in 2D, we neglect excluded volume, which is reasonable since the F-actin density in our simulations is well below the isotropic to nematic transition, so the network connectivity dominates the dynamics. The model is described in detail in Section S1, and Table S1 lists all simulation parameters.

Self-assembly and characterization of actin network structures. We observe three distinct network architectures formed from initially disordered mixtures of F-actin, motors, and crosslinkers: bundled, polarity-sorted, and contracted. Examples of each structure are shown for simulations of 500 10 μm long filaments in the highlighted corners of Fig. 1. When F-actin is mixed with crosslinkers, a bundled network forms as crosslinkers bind proximal F-actin into thick bundles, which in turn are joined at intersections to yield a well-connected mesh. When F-actin is mixed with motors, barbed ends aggregate to form a polarity-sorted network. Combining F-actin with both motors and crosslinkers results in macroscopic contraction of the actin filaments into dense and disconnected aggregates.

To systematically explore how varying constituent network properties affects structure formation, we introduce physical order parameters to quantify each of the observed structural phases. We compute the spatial extent of F-actin aggregation using the radial distribution function, $g(r) = P(r)/(2\pi r\delta r\rho_a)$, where $P(r)$ is the probability that two actin beads are separated by a distance in the range $[r, r+\delta r]$, (here, $\delta r = 0.05$ μm) and ρ_a is the number density of actin beads. For a homogeneous network, $g(r) \approx 1$ at all distances (Fig. 2A; the small peaks at integer r arise from the spacing of beads within actin filaments). In contrast, for contracted networks, $g(r) \gg 1$ for $r < 10$ μm, indicating F-actin exceeds the bulk density.

While Fig. 2A shows that actin filaments are nearly uniformly distributed in a polarity-sorted network, Fig. 1 indicates that their barbed ends (blue) are concentrated. To quantify their aggregation specifically, we compute the ratio $g(r_{barb})/g(r)$, where r_{barb} is the distance between filament barbed ends. Fig. 2B shows that in polarity-sorted networks F-actin barbed ends are aggregated (and have a secondary peak at 0.5 μm, the rest length of motors). In contracted networks, barbed ends also aggregate to a higher degree than bundled networks, indicating a degree of polarity sorting.

Fig. 2A indicates that bundled networks aggregate at smaller length scales, ~ 0.1 μm, corresponding to the crosslinker rest length $l_{xl} = 0.15$ μm. To quantify the degree of bundling, and to distinguish it from contractility, we measure the distribution of network pore sizes by a procedure that is similar in spirit but simpler than that in Ref. 35. Namely, we grid the simulation box into $(0.25\ \mu\text{m})^2$ bins and compute how many filaments pass through each bin. For each empty bin, we determine the lengths of the contiguous stretches of empty bins that contain it in the vertical and horizontal directions (Fig. S2). We average these lengths over all empty bins to obtain an average mesh size for each network structure.

In Fig. 2C, the distributions of mesh sizes for polarity-sorted and homogeneous networks are similar, indicating that the former does not coarsen significantly. The bundled and contracted networks exhibit larger pore sizes; indeed, contracted networks exhibit pore sizes spanning the simulation region, indicating that the network has ripped apart. We can distinguish these cases by normalizing the mesh size by $\langle g(r)\rangle = R^{-1}\int_0^R g(r)dr$ ($R = 5$ μm), which quantifies the extent of aggregation. The inset shows that, while the contracted networks initially bundle, at long times this effect is small compared to aggregation. In contrast, bundled networks have a continuously increasing normalized mesh size (Fig. 2C, inset); we take this measure as a metric for the degree of bundling.

To examine the relationship between actin network structure and contractility, we use the metric $\langle \nabla \cdot \mathbf{v}\rangle$, where $\mathbf{v}$ is the actin's velocity field, and $\langle ...\rangle$ indicates spatial averaging (Section S3) [20]. As shown in Fig. 2D, $\langle \nabla \cdot \mathbf{v}\rangle$ becomes significantly more negative for aggregating networks than for bundling or polarity-sorted networks. Comparison with Fig. 2A shows that extensive contractility is associated with large $g(r)$.

Using these order parameters, we map the structural phase space of actomyosin networks as functions of motor and crosslinker densities and their binding affinities (Fig. 3). Consistent with Fig. 1, networks are contracted when motor and crosslinker densities are high (Fig. 3A), polarity-sorted when only motor density is high (Fig. 3B), and bundled when only crosslinker density is high (Fig. 3C). Interestingly, while high motor densities inhibit bundling, a small population of motors ($\rho_m \approx 0.02$ μm^{-2}) enhances filament bundling.

Non-monotonic trends in binding kinetics and filament length. Finally, we modulate molecular-level interaction parameters between F-actin and its binding partners (crosslinkers, motors) to dissect their relative roles in building different structures. These parameters are hard to change independently in experiment. At fixed motor and crosslinker densities, we find that cytoskeletal structures can be tuned by varying the dissociation constants, $k^{\text{off}}_{m(xl)}$ (Fig. 3D-F). The trends are non-monotonic, in contrast to those in the densities (Fig. 3A-C). In particular, contraction is highest for intermediate values of $k^{\text{off}}_{m,xl}$ (Fig. 3D), and bundling is highest for low values of k^{off}_{xl} with low or high k^{off}_m (Fig. 3F). Notably, this non-

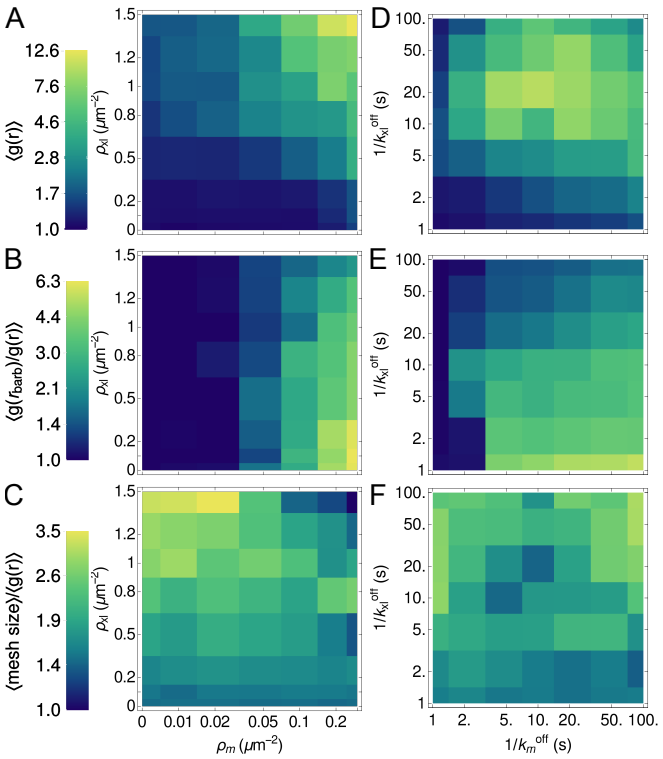

FIG. 3. Maps of network properties. Colors indicate the values of order parameters characterizing network contractility (A,D), polarity sorting (B,E), and bundling (C,F), at constant filament length, $L = 10$ μm, binding affinity $k^{\text{off}}_m = k^{\text{off}}_{xl} = 0.1$ s^{-1} (left), and densities $\rho_m = 0.2$ μm^{-2}, $\rho_{xl} = 1$ μm^{-2} (right; structures shown in Fig. S5). All averages are over the last 50 s of 4 simulations of 400 s; order parameters that are functions of distance, e.g., $g(r)$, are integrated over $0 < r \leq 5$ μm.

monotonic trend only arises for a fixed simulation time, t_F. For a fixed value of $t_F k^{\text{off}}_{m(xl)}$, changing $1/k^{\text{off}}_{m(xl)}$ modulates structure formation in a monotonic manner, akin to changing $\rho_{m(xl)}$ (Fig. S3). The non-monotonic trends are important, however, because many structures in cells must form transiently due to competing kinetic processes, such as actin filament turnover [7, 36].

As the length (L) of F-actin varies considerably within cells [37], we tested how varying L and $k^{\text{off}}_{m(xl)}$ in tandem affects structure formation. In Fig. 4A, we show that when mixed with both motors and crosslinkers, longer actin filaments yield larger contracted aggregates. This is due to an increase in network connectivity for longer filaments; filaments that are too short do not undergo significant aggregation. As in Fig. 3B, the dependence of aggregation on binding affinity is non-monotonic whenever there is significant aggregation (i.e., $L \geq 5$ μm). In Fig. 4B, we show that for networks with only motors, at low k^{off}_m, increasing filament length promotes polarity sorting. By contrast, high k^{off}_m, completely suppresses polarity sorting due to the short lifetime of motor attachment. As evident from the representative network

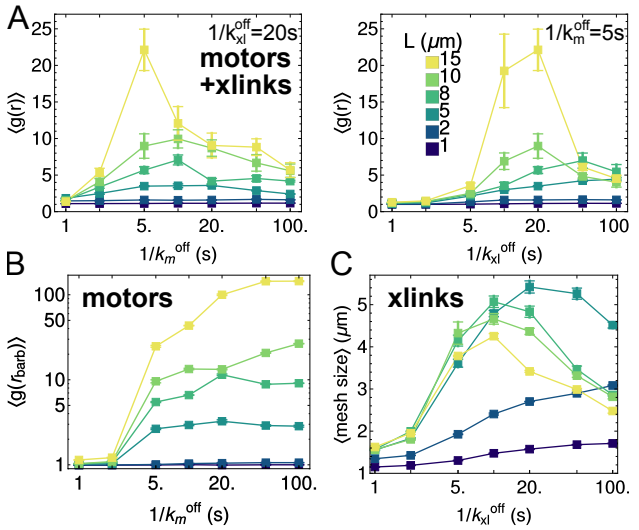

FIG. 4. Effects of varying motor and crosslinker affinities for filaments of different lengths, L. (A) At $\rho_m = 0.2\ \mu\text{m}^{-2}$ and $\rho_{xl} = 1\ \mu\text{m}^{-2}$, contractility is maximized at finite values of k_m^{off} and k_{xl}^{off} for $L \geq 5\ \mu$m. (B) For assemblies of F-actin and motors, polarity sorting generally increases with higher L and higher $1/k_m^{\text{off}}$. (C) For passively crosslinked F-actin, there is an optimal k_{xl}^{off} and L for maximizing the mesh size. Normalizing quantities in (B) and (C) with respect to $\langle g(r)\rangle$ does not change these conclusions (Fig. S4). Error bars are standard error of the mean.

structures in Fig. S6, making the filaments short also suppresses polarity sorting. Both the large number of filaments and their rapid diffusion favor mixing over the consistent motor-filament interactions needed for sorting.

For networks with only crosslinkers, the mesh size (Fig. 4C) is non-monotonic with respect to both filament length and crosslinker affinity. From example structures (Fig. S7), we see that low crosslinker affinity and short filament lengths cause mixing for the same reasons as immediately above, such that stable crosslinked networks do not form. Conversely, assemblies with high crosslinker affinity or long filament lengths form crosslinked networks, but they rearrange slowly, so further coarsening is impeded, and the mesh size remains small. As these non-monotonic trends only occur for $L > 5\ \mu$m, they are more likely to impact structures with longer actin filaments found in budding yeast [38], stereocilia [39], filopodia, or *in vitro* reconstituted networks [17, 22]. Structures with shorter filaments, as found in lamellipodia or the actin cortex ($< 2\ \mu$m) [16, 40], are less likely to have a finite binding affinity that maximizes contractility.

Structure of networks tunes transport and force propagation. While the structures of contracted, polarity-sorted, and bundled networks clearly differ, their consequences for biophysical functions are not immediately apparent. To determine how these structures influence motor transport [10, 41], we fix the actin structures and follow the dynamics of the motors. This facilitates obtaining well-converged statistics for the dynamics and interpretation in terms of individual trajectories. While the apparent scaling of the mean-squared displacement is consistent with simple diffusion (Fig. S8A), as observed experimentally [42], sample trajectories (Fig. S8C) indicate that motors in contracted and polarity-sorted structures spend significant amounts of time trapped in aggregates of barbed ends. We quantify this caging effect using a previously defined metric that can distinguish different kinds of motion [42]. Namely, we compute the velocity of a motor with center of mass position $\vec{r}_m(t)$ at time t as $\vec{v}_m(t,\Delta) = \vec{r}_m(t+\Delta) - \vec{r}_m(t)$ and evaluate the distribution of angles, θ, between consecutive velocity vectors $\vec{v}_m(t,\Delta)$ and $\vec{v}_m(t+\Delta,\Delta)$, at different values of Δ.

We find that for all structures, there is at least one time scale in which the distribution has a broad peak at $\theta = \pi$ (Fig. 5A), indicating that motors are reversing direction, consistent with confinement. For polarity-sorted networks barbed ends are most tightly aggregated, and thus motors exhibit caging at all time scales measured. Contracted networks are partially polarity-sorted, so filaments can direct motors both in and out of aggregates, making the caging more spatially extended. Because it takes longer to explore the extended length scale, the caging manifests only at $\Delta \gtrsim 50$ s. Bundled networks show caging effects most prominently at intermediate time scales. In this case, the caging corresponds to motors cycling between oppositely oriented filaments, which can give rise to apparently glassy dynamics [32].

Next, we evaluated how structural rearrangements in actin networks affect their ability to propagate mechanical forces over long length scales. To this end, we subjected the final network configuration to a shear strain of magnitude $\gamma = 0.5$ (Section S8) and measured the resulting strain energy. In Fig. 5B, we show the strain dependence of the total strain energy density, $w = (U_f + U_m + U_{xl})/V$, where U_f, U_m, and U_{xl} are the potential energies of the F-actin, motors, and crosslinkers, respectively, (Section S1) and $V = 250\ \mu\text{m}^3$ is the simulation box volume, assuming a thickness of 0.1 μm. Bundled networks exhibit a quadratic dependence on strain, indicating a solid-like material response. By contrast, contracted and polarity-sorted networks are fragile, with linear dependences of energy density on strain.

Discussion. Our coarse-grained simulations show how modulating the abundance and properties of cytoskeletal constituents can tune emergent network structures. For finite times, we find that motor and crosslinker binding affinities, as well as filament lengths, have optimal values for maximizing contractility, bundling, and polarity sorting. While there are still many unanswered questions on the self-organized mechanical behavior of cytoskeletal materials, our work takes an important step forward by linking kinetics to the selection of network structures with specific mechanical functions. We expect that the order parameters that we introduced to characterize network structure can also be applied to interpretation of experimental imaging data. Further simulations using our modeling framework can shed light on

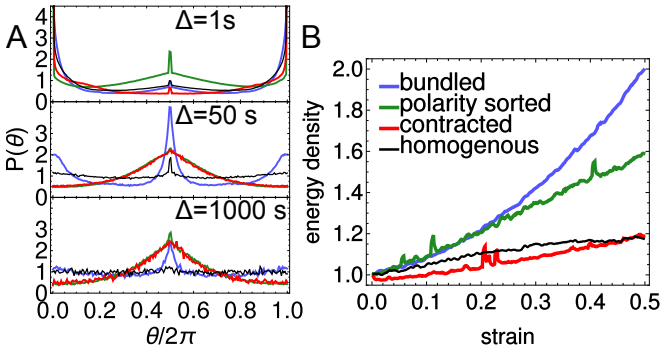

FIG. 5. Functional consequences of the network structures highlighted in Fig. 1. (A) Distributions of angles between subsequent velocity vectors of tracer motors for different lag times, Δ, show motor caging at varying time scales for bundled, polarity-sorted, and contracted networks, and underdamped diffusion for homogeneous networks [42]. The small spikes at $\theta = \pi$ in some simulations result from the fact that motors cannot walk off filaments, and we show in Fig. S9 that these features can be suppressed by increasing the off rate at filament ends. (B) Energy density w of actin networks as a function of their strain (shown normalized by their unstrained energy densities) demonstrates network elasticity. Fitting the unnormalized curves to a quadratic function yields a shear modulus of $G \approx 0.66$ Pa for the bundled network (within the range of experimentally measured values for actin-filamin networks [21]) and $G \approx 0$ for the other networks.

the structure-function relations in other active polymer assemblies, including networks of microtubules, kinesin, and dynein [43, 44]. From the perspective of materials design, our work demonstrates how a limited set of molecular building blocks can self-assemble diverse active materials. This presents the prospect that theory and simulation can be used to guide the design of active biomimetic materials with desired collective mechanical properties.

ACKNOWLEDGMENTS

We thank M. Gardel, J. Weare, S. Stam, and K. Weirich for helpful conversations. This research was supported in part by the University of Chicago Materials Research Science and Engineering Center (NSF Grant No. 1420709). S.L.F. was supported by the DoD through the NDSEG Program. G.M.H. was supported by an NIH Ruth L. Kirschstein NRSA award (1F32GM113415-01). S.B. was supported by a UCL Strategic Fellowship. Simulations resources were provided by the Research Computing Center at the University of Chicago.

[1] M. Murrell, P. W. Oakes, M. Lenz, and M. L. Gardel, Nat. Rev. Mol. Cell Biol. **16**, 486 (2015).
[2] A. Michelot and D. G. Drubin, Curr. Biol. **21**, R560 (2011).
[3] T. D. Pollard and G. G. Borisy, Cell **112**, 453 (2003).
[4] A. J. Lomakin, K.-C. Lee, S. J. Han, D. A. Bui, M. Davidson, A. Mogilner, and G. Danuser, Nat. Cell Biol. **17**, 1435 (2015).
[5] J. T. Parsons, A. R. Horwitz, and M. A. Schwartz, Nat. Rev. Mol. Cell Biol. **11**, 633 (2010).
[6] J. Sedzinski, M. Biro, A. Oswald, J.-Y. Tinevez, G. Salbreux, and E. Paluch, Nature **476**, 462 (2011).
[7] E. Munro, J. Nance, and J. R. Priess, Dev. Cell **7**, 413 (2004).
[8] S. A. Tabei, S. Burov, H. Y. Kim, A. Kuznetsov, T. Huynh, J. Jureller, L. H. Philipson, A. R. Dinner, and N. F. Scherer, Proc. Natl. Acad. Sci. U.S.A **110**, 4911 (2013).
[9] P. M. Bendix, G. H. Koenderink, D. Cuvelier, Z. Dogic, B. N. Koeleman, W. M. Brieher, C. M. Field, L. Mahadevan, and D. A. Weitz, Biophys. J. **94**, 3126 (2008).
[10] S. Kohler, V. Schaller, A. Bausch, *et al.*, Nat. Mater. **10**, 462 (2011).
[11] J. Alvarado, M. Sheinman, A. Sharma, F. C. MacKintosh, and G. H. Koenderink, Nat Phys **9**, 591 (2013).
[12] M. P. Murrell and M. L. Gardel, Proc. Natl. Acad. Sci. USA **109**, 20820 (2012).
[13] M. Murrell and M. L. Gardel, Mol. Biol. Cell **25**, 1845 (2014).
[14] H. Ennomani, G. Letort, C. Guérin, J.-L. Martiel, W. Cao, F. Nédélec, M. Enrique, M. Théry, and L. Blanchoin, Curr. Biol. **26**, 616 (2016).
[15] I. Linsmeier, S. Banerjee, P. W. Oakes, W. Jung, T. Kim, and M. Murrell, Nat. Commun. **7**, 12615 (2016).
[16] P. Chugh, A. G. Clark, M. B. Smith, D. A. Cassani, K. Dierkes, A. Ragab, P. P. Roux, G. Charras, G. Salbreux, and E. K. Paluch, Nat. Cell Biol. **19**, 689 (2017).
[17] S. Stam, S. L. Freedman, S. Banerjee, K. L. Weirich, A. R. Dinner, and M. L. Gardel, Proc. Natl. Acad. Sci. U.S.A **114**, E10037 (2017).
[18] M. Gardel, J. Shin, F. MacKintosh, L. Mahadevan, P. Matsudaira, and D. Weitz, Science **304**, 1301 (2004).
[19] K. Kasza, G. Koenderink, Y. Lin, C. Broedersz, W. Messner, F. Nakamura, T. Stossel, F. MacKintosh, and D. Weitz, Phys. Rev. E **79**, 041928 (2009).
[20] S. L. Freedman, S. Banerjee, G. M. Hocky, and A. R. Dinner, Biophys. J **113**, 448 (2017).
[21] K. Schmoller, O. Lieleg, and A. Bausch, Biophys. J. **97**, 83 (2009).
[22] K. L. Weirich, S. Banerjee, K. Dasbiswas, T. A. Witten, S. Vaikuntanathan, and M. L. Gardel, Proc. Natl. Acad. Sci. U.S.A **114**, 2131 (2017).
[23] O. Lieleg, R. M. Baumgärtel, and A. R. Bausch, Biophys. J. **97**, 1569 (2009).
[24] K. Kruse, J.-F. Joanny, F. Jülicher, J. Prost, and K. Sekimoto, Eur. Phys. J. E Soft Matter **16**, 5 (2005).
[25] M. Lenz, T. Thoresen, M. L. Gardel, and A. R. Dinner, Phys. Rev. Lett. **108**, 238107 (2012).
[26] J. Prost, F. Jülicher, and J. Joanny, Nat. Phys. **11**, 111 (2015).

[27] N. L. Dasanayake, P. J. Michalski, and A. E. Carlsson, Phys. Rev. Lett. **107**, 118101 (2011).
[28] S. Wang and P. G. Wolynes, Proc. Natl. Acad. Sci. USA **109**, 6446 (2012).
[29] J. M. Belmonte, M. Leptin, and F. Nédélec, Molecular Syst. Biol. **13**, 941 (2017).
[30] T. Kim, W. Hwang, H. Lee, and R. D. Kamm, PLoS Comput. Biol. **5**, e1000439 (2009).
[31] D. A. Head, G. Gompper, and W. J. Briels, Soft Matter **7**, 3116 (2011).
[32] M. Scholz, S. Burov, K. L. Weirich, B. J. Scholz, S. A. Tabei, M. L. Gardel, and A. R. Dinner, Phys. Rev. X **6**, 011037 (2016).
[33] C. Cyron, K. Müller, K. Schmoller, A. Bausch, W. Wall, and R. Bruinsma, Europhys. Lett. **102**, 38003 (2013).
[34] T. C. Bidone, W. Jung, D. Maruri, C. Borau, R. D. Kamm, and T. Kim, PLoS Comput. Biol. **13**, e1005277 (2017).
[35] W. Mickel, S. Münster, L. M. Jawerth, D. A. Vader, D. A. Weitz, A. P. Sheppard, K. Mecke, B. Fabry, and G. E. Schröder-Turk, Biophys. J. **95**, 6072 (2008).
[36] M. Fritzsche, C. Erlenkämper, E. Moeendarbary, G. Charras, and K. Kruse, Sci. Adv. **2**, e1501337 (2016).
[37] L. Mohapatra, B. L. Goode, P. Jelenkovic, R. Phillips, and J. Kondev, Annu. Rev. Biophys. **45**, 85 (2016).
[38] M. Chesarone-Cataldo, C. Guérin, H. Y. Jerry, R. Wedlich-Soldner, L. Blanchoin, and B. L. Goode, Dev. Cell **21**, 217 (2011).
[39] H. W. Lin, M. E. Schneider, and B. Kachar, Curr. Opin. Cell Biol. **17**, 55 (2005).
[40] G. Salbreux, G. Charras, and E. Paluch, Trends Cell Biol. **22**, 536 (2012).
[41] C. M. Brawley and R. S. Rock, Proc. Natl. Acad. Sci. U.S.A **106**, 9685 (2009).
[42] S. Burov, S. A. Tabei, T. Huynh, M. P. Murrell, L. H. Philipson, S. A. Rice, M. L. Gardel, N. F. Scherer, and A. R. Dinner, Proc. Natl. Acad. Sci. USA **110**, 19689 (2013).
[43] T. Sanchez, D. T. Chen, S. J. DeCamp, M. Heymann, and Z. Dogic, Nature **491**, 431 (2012).
[44] P. J. Foster, S. Fürthauer, M. J. Shelley, and D. J. Needleman, eLife **4** (2015).

Supplemental Materials for Design principles for selective self-assembly of active networks

Simon L. Freedman, Glen M. Hocky, Shiladitya Banerjee, Aaron R. Dinner

S1. AFINES SIMULATION

In AFINES, actin filaments, myosin motors, and passive crosslinker proteins are modeled as coarse grained entities. Actin filaments are treated as worm-like chains of $N+1$ beads connected by N harmonic springs (links) and $N-1$ angular harmonic springs. Thus, the internal forces on an actin filament can be obtained from the gradient of the potential energy U_f:

$$U_f = \frac{k_a}{2}\sum_{i=1}^{N}(|\vec{r}_i - \vec{r}_{i-1}| - l_a)^2 + \frac{\kappa_B}{2l_a}\sum_{i=2}^{N}\theta_i^2, \tag{S1}$$

where $\vec{r}_i$ is the position of the i^{th} bead on a filament, θ_i is the angle between the i^{th} and $(i-1)^{th}$ links, k_a is the stretching force constant, κ_B is the bending modulus, and l_a is the equilibrium length of a link. The persistence length of the filament is then $L_p = \kappa_B/k_BT$, where k_B is Boltzmann's constant and T is the temperature.

We model crosslinkers as Hookean springs, with two ends (heads) that can stochastically bind to and unbind from filaments. Thus, the potential energy of a crosslinker is

$$U_{xl} = \frac{1}{2}k_{xl}(|\vec{r}_1 - \vec{r}_2| - l_{xl})^2 - k_BT\ln(k_{xl}^{\text{on}}/k_{xl}^{\text{off}})(I_1 + I_2) \tag{S2}$$

where k_{xl} is the crosslinker stiffness, l_{xl} is its rest length, $\vec{r}_{1(2)}$ is the position of head 1(2), $I_{1(2)}$ is 1 if head 1(2) is bound and 0 otherwise, and $k_{xl}^{\text{on}}(k_{xl}^{\text{off}})$ is the rate constant for binding (unbinding). When a crosslinker is bound, it moves with the filament to which it is bound. When both crosslinker heads are bound, its tensile force, $\vec{F}_{xl}$ is propagated onto the filament beads neighboring each bound head at position $\vec{r}_{xl}$ via the lever rule,

$$\vec{F}_i = \vec{F}_{xl}\frac{|\vec{r}_{i+1} - \vec{r}_{xl}|}{|\vec{r}_{i+1} - \vec{r}_i|} \quad \text{and} \quad \vec{F}_{i+1} = \vec{F}_{xl} - \vec{F}_i, \tag{S3}$$

where $\vec{F}_i$ is the force on the filament bead at position $\vec{r}_i$.

Binding and unbinding are governed by a Monte Carlo procedure constructed to satisfy detailed balance in the absence of motors. At each timestep of duration Δt, an unbound crosslinker head becomes bound to the i^{th} nearby filament with probability $k_{xl}^{\text{on}}\Delta t P_i$, where P_i is defined as follows. The closest point on the filament is identified, and the change in energy associated with moving the head to it, ΔU_i is computed; $P_i = \min[1, \exp(-\Delta U_i/k_BT)]$. When a head becomes bound, its displacement, in the frame of reference of the filament link to which it attached, is stored as $\Delta\vec{r}$. Later, the head can become unbound with probability $k_{xl}^{\text{off}}\Delta t P$, where $P = \min[1, \exp(-\Delta U/k_BT)]$ and ΔU is the energy that would result from applying a displacement of $-\Delta\vec{r}$ to the head.

We model a motor similarly to a crosslinker, in that it is a Hookean spring, can bind to and unbind from filaments, and propagates force onto them. Thus, their potential energy is identical to Eq. S2 with the subscript m replacing the subscript xl. Additionally, a bound motor head moves towards the barbed end of the actin filament to which it is bound at a load dependent velocity

$$v(F_m) = v_0 \max\left[1 + \frac{\vec{F}_m \cdot \hat{r}}{F_s}, 0\right], \tag{S4}$$

where v_0 is the unloaded motor speed, $\vec{F}_m = -k_m(|\vec{r}_1 - \vec{r}_2| - l_m)$ is the tensile force on the motor, and $\hat{r}$ is the tangent to the filament at the point where the motor is bound; $\hat{r}$ points toward the pointed end of the filament.

We simulate the system using Brownian dynamics such that the position of an actin bead, motor head, or crosslinker head at time t is generated by the equation

$$\vec{r}(t+\Delta t) = \vec{r}(t) + \vec{F}(\vec{r}(t))\mu\Delta t + \sqrt{\frac{k_BT\mu\Delta t}{2}}\left(\vec{W}(t+\Delta t) + \vec{W}(t)\right), \tag{S5}$$

where $\vec{F}(\vec{r}(t))$ is the gradient of the potential of the particle, $\vec{W}(t)$ is a vector of random numbers drawn from the standard normal distribution, and we use the Stokes relation $\mu = 1/(6\pi R\nu)$ in the damping term, where R is the size

Symbol	Description (units) [ref]	Value
	Actin Filaments	
ρ_l	link density (μm^{-2})	2
N_l	number of links per filament (L/l_a)	$[1, 15]$
l_a	link rest length (μm) [S2]	1
k_a	stretching force constant (pN/μm)	5
κ_B	bending modulus (pNμm^2) [S3]	0.068
	Myosin Minifilaments	
ρ_m	density (μm^{-2})	$[0, 0.3]$
l_m	rest length (μm) [S4]	0.5
k_m	stiffness (pN/μm)	1
k_m^{on}	maximum attachment rate (s^{-1})	1
k_m^{off}	maximum detachment rate (s^{-1})	$[0.01, 1]$
k_m^{end}	maximum end detachment rate (s^{-1})	$[0.01, 1]$
v_0	unloaded speed (μm/s) [S5]	1
F_s	stall force of myosin (pN) [S6]	0.5
	Crosslinkers	
ρ_{xl}	density (μm^{-2})	$[0, 1.5]$
l_{xl}	rest length (filamin) (μm) [S7]	0.15
k_{xl}	stiffness (pN/μm)	1
k_{xl}^{on}	maximum attachment rate (s^{-1})	1
k_{xl}^{off}	maximum detachment rate (s^{-1})	$[0.01, 1]$
	Environment	
Δt	dynamics timestep (s)	0.00002
t_F	maximum simulated time (s)	400
X, Y	length and width of assay (μm)	50
g	grid density (μm^{-1})	2.5
T	temperature (K)	300
ν	dynamic viscosity (Pa·s)	0.001

TABLE S1. Parameter Values

of the particle, and ν is the dynamic viscosity of its environment [S1]. We simulate the system in 2D and use periodic boundary conditions to limit boundary effects. A complete list of model parameters used for Figs. 1-4 is provided in Table S1 and additional methods used for Fig. 5 are described below (Sections S7 and S8).

S2. VARYING MOTOR AND CROSSLINKER DENSITIES

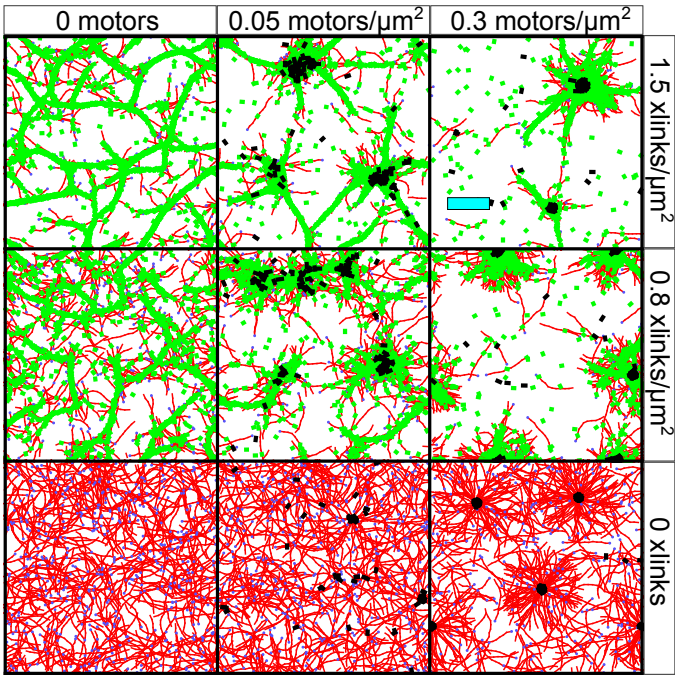

FIG. S1. Same as Fig. 1, but with motors (black) and crosslinkers (green) also shown on top of actin (red, barbed end marked by blue dot). Cyan scale bar is 10 μm. Parameters held constant: $L = 10$ μm, $k_{xl(m)}^{\text{off}} = 0.1$ s^{-1}.

S3. ACTIN VELOCITY FIELD CALCULATION

Contraction of actin networks is typically calculated by identifying sinks in the divergence of the actin velocity field. To construct this field, we first calculate the velocity of actin beads $\vec{v}_a = (\vec{r}_a(t+h) - \vec{r}_a(t))/h$ where $\vec{r}_a(t)$ is the position of an actin bead at time t, and h is the lag time. To reduce noise, we calculate $\vec{v}_k(\vec{r_k})$, the average velocity in every bin k of size Δr^2. We then interpolate the velocity field using Gaussian Radial Basis Functions (RBF), such that the velocity at any position $\vec{r}$ is

$$\vec{v}(\vec{r}) = \sum_{k=1}^{M} \vec{w}_k e^{-(|\vec{r}-\vec{r}_k|/\epsilon)^2}, \tag{S6}$$

where M is the number of bins with at least 10 actin beads, and $\vec{w}_k$ are the weights of the basis functions, determined by solving the equation $\vec{v}(\vec{r_k}) = \vec{v_k}(\vec{r_k})$ (using the scipy.interpolate.Rbf package [S8]). For Fig. 2B, we used a lag time of $h = 10$ s, a threshold of $n = 10$ actin beads in a local box of size $\Delta r = 5$ μm and a Gaussian width of $\epsilon = 5$ μm, as we have found these interpolation values robustly capture the motion of the actin [S9].

Because of the periodic boundary conditions, there is no flux of actin into the simulation cell, and $\langle \nabla \cdot \vec{v}(r) \rangle = 0$. Therefore, to measure contraction, we threshold the divergence by the local actin density and only total the divergence from 1 μm^2 patches that contain more than 5 actin beads in Fig. 2D, as in Ref. S17.

S4. MESH SIZE

We show an example of the results of the mesh size calculation described in the main text on a bundled network at $t = 400$ s.

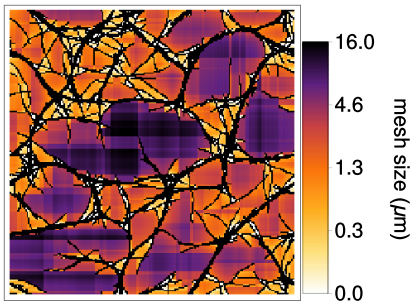

FIG. S2. Actin is shown in black and the size of the local mesh corresponds to the depth of color.

S5. EFFECTS OF RELAXATION TIMES ON NETWORK STRUCTURES

To understand how the structure-parameter relations that we elucidated depended on the observation time, we measured the magnitude of contraction at a fixed value of $k^{\text{off}}_{m(xl)}t$. We find that fixing $k^{\text{off}}_{m(xl)}t$ yields a monotonic decrease in contraction (Fig. S3A), indicating that for long times, *total* contraction (as opposed to the rate of contraction) is maximized by increasing the affinity of motors and crosslinkers with F-actin. In contrast to contraction, for networks without crosslinkers, polarity sorting decreases monotonically with decreasing motor affinity (Fig. S3B). However, for networks without motors, at fixed times bundling is maximized for intermediate k^{off}_{xl}, while at long times it is maximized at low k^{off}_{xl} (Fig. S3C). Our results indicate that to attain specific structures within a fixed time scale, there are optimal choices for motor and crosslinker affinities, while at long times $1/k^{\text{off}}_{m(xl)}$ affects structure formation similarly to $\rho_{m(xl)}$.

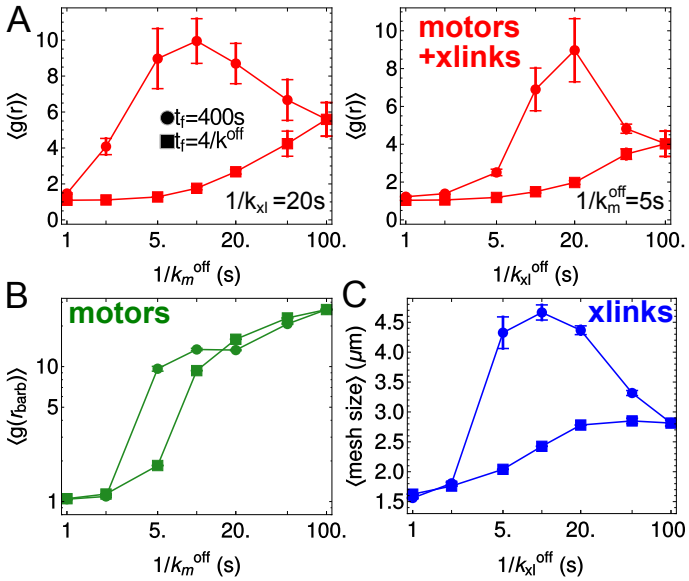

FIG. S3. The effects of varying motor and crosslinker affinities for $L = 10$ μm. (A) For a system with both motors and crosslinkers ($\rho_m = 0.3$ μm^{-2} and $\rho_{xl} = 1.5$ μm^{-2}) there is an optimal k_m^{off} (left) and k_{xl}^{off} (right) for maximal contraction in a fixed time interval. Amount of contraction decreases at constant $k_{m(xl)}^{\text{off}} t$, indicating that decreasing $k_{m(xl)}^{\text{off}}$ is similar to increasing $\rho_{m(xl)}$. (B) For assemblies of F-actin and motors ($\rho_m = 0.3$ μm^{-2}), polarity sorting decreases with decreasing k_m^{off}. (C) For passive crosslinked F-actin, there is an optimal k_{xl}^{off} for bundle formation in a fixed time. For fixed $k_{xl}^{\text{off}} t_F$, the amount of bundling decreases monotonically with increasing k_{xl}^{off}.

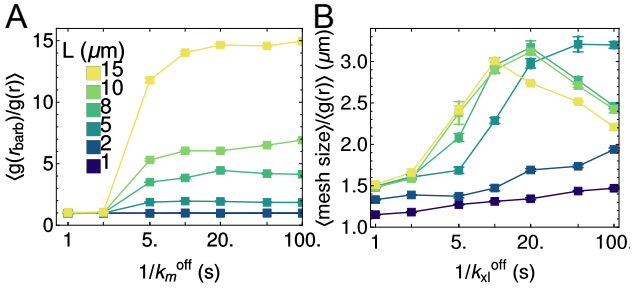

FIG. S4. Same as Fig. 4B-C but normalized by $\langle g(r) \rangle$

S6. STRUCTURE EXAMPLES

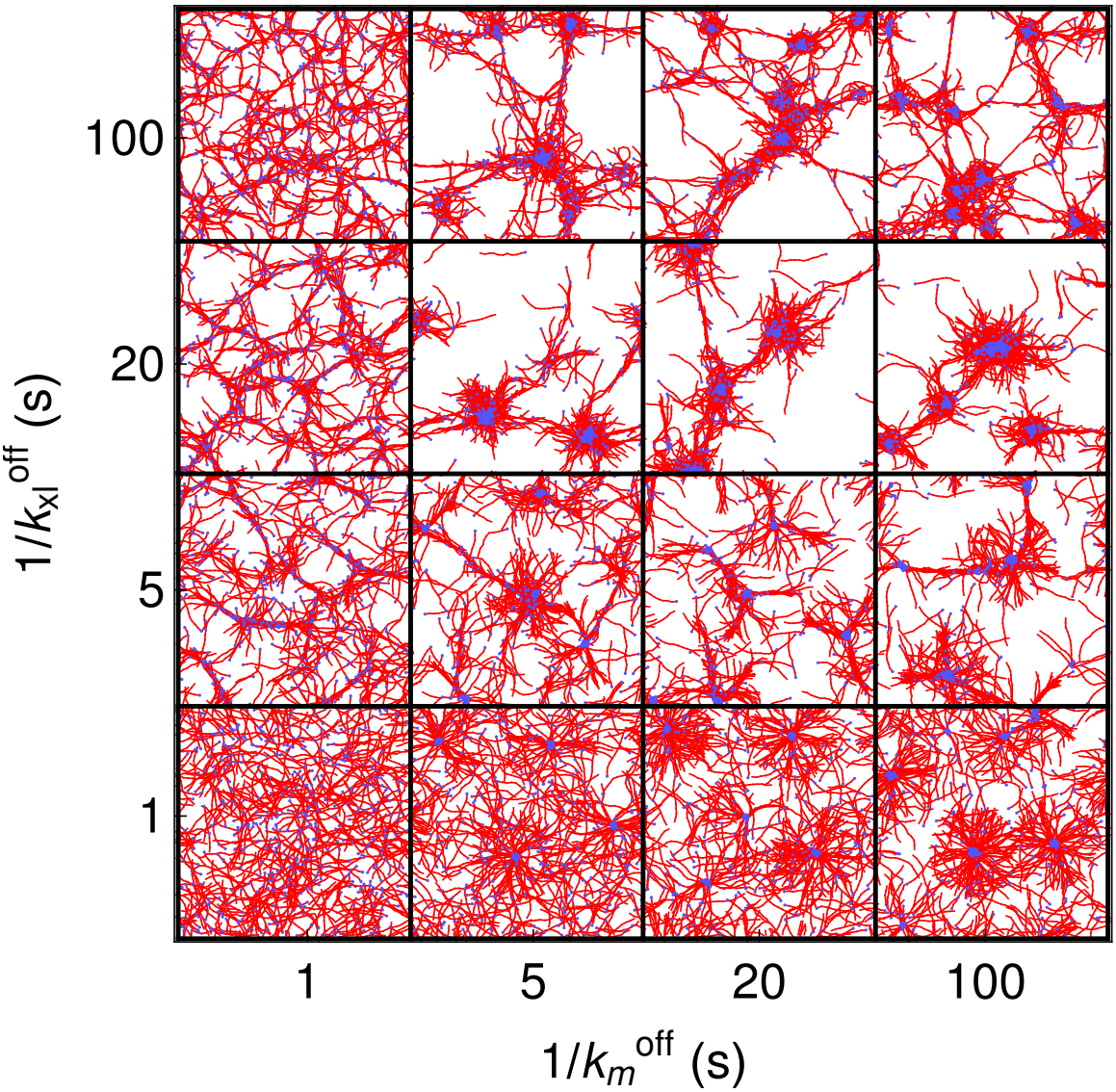

FIG. S5. Sample structures after 400 s simulation, for varying motor and crosslinker off rates. Parameters held constant: $\rho_m = 0.2$ μm^{-2}, $\rho_{xl} = 1$ μm^{-2}, $L = 10$ μm. Motors and crosslinkers not shown for clarity.

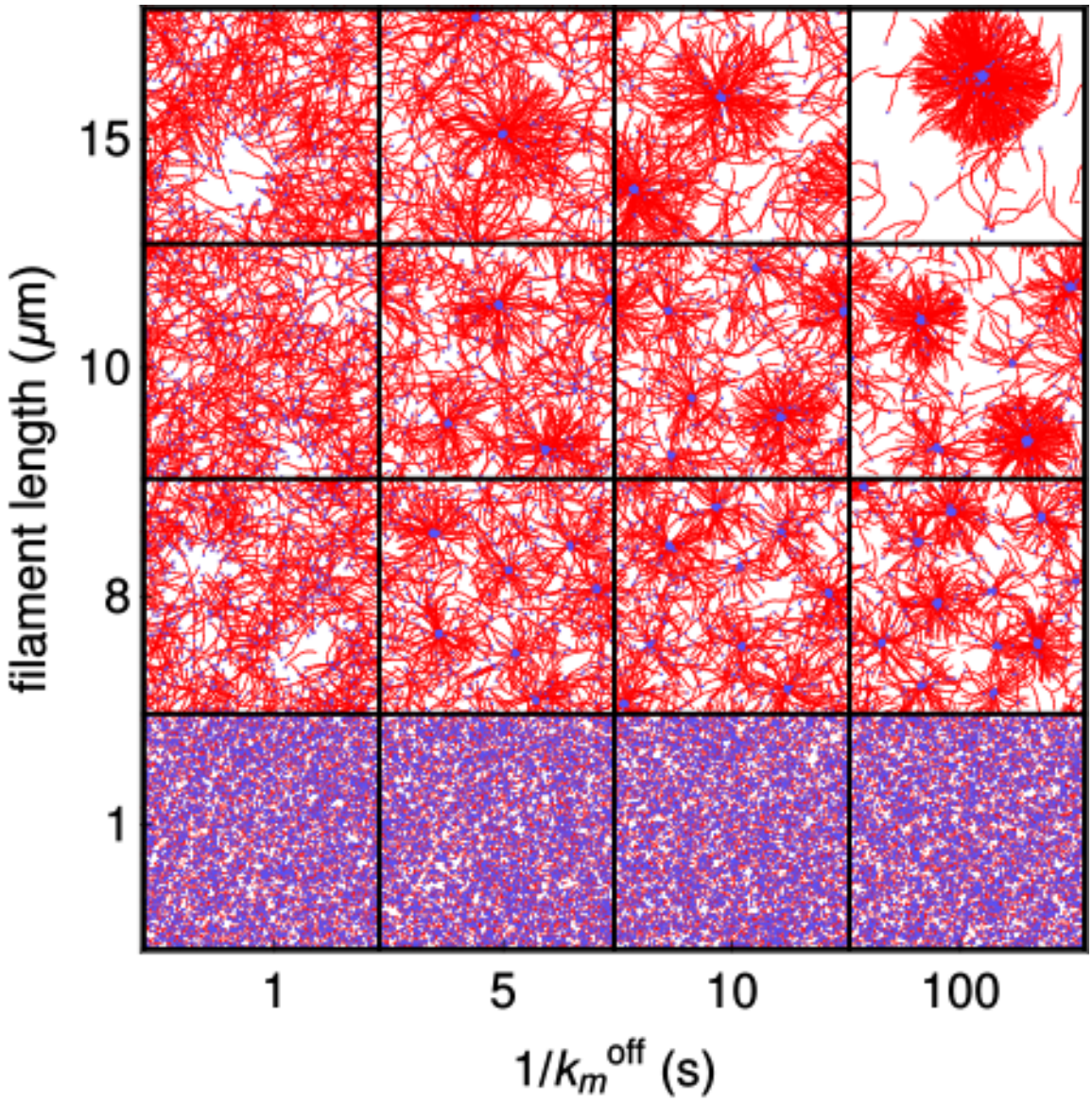

FIG. S6. Sample structures after 400 s simulation, for varying filament length and motor off rate. Parameters held constant: $\rho_m = 0.3\ \ \mu\text{m}^{-2}$, $\rho_{xl} = 0$. Motors and crosslinkers not shown for clarity.

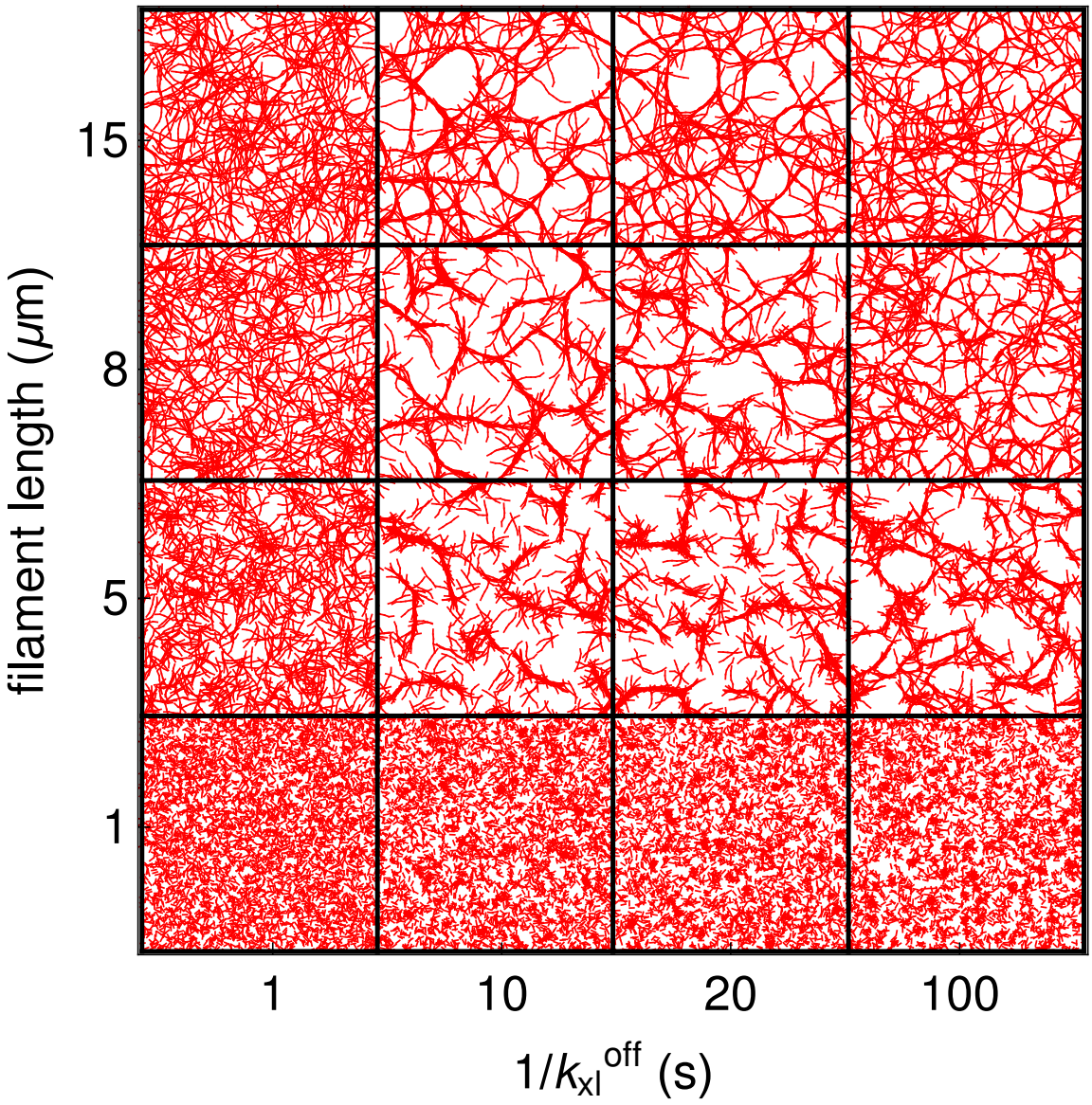

FIG. S7. Sample structures after 400 s simulation, for varying filament length and crosslinker off rate. Parameters held constant: $\rho_m = 0$, $\rho_{xl} = 1.5\ \ \mu\text{m}^{-2}$. Motors, crosslinkers, and barbed ends not shown for clarity.

S7. EFFECTS OF STRUCTURE ON MOTOR TRANSPORT

To quantify the ability of networks to direct motor transport, we added 1250 motors at random locations to all three structural phases (i.e., their structures at $t_F = 400$ s) and simulated for an additional 30000 s. In Fig. S8A-B, we plot the mean squared displacement as a function of lag time, Δ, and show that for all phases, this quantity increases linearly, indicating that the motor trajectories are, on average, diffusive. We performed this measurement with the motors described above (Section S1), as well as ones that detach faster from the barbed ends of filaments; i.e., at the barbed end they had a detachment rate of $k_m^{\text{end}} = 100k_m^{\text{off}}$ [S9]. This second set of measurements was done to ascertain that the observed motor caging was a consequence of network structure, and not a consequence of dwelling at the barbed ends of the filaments, given that we assume a uniform detachment rate. Both types of motors display caging effects in their trajectories (Fig. S8C), which we have quantified using the distribution of angles between consecutive velocity measurements at varying lag times (Fig. 5A and Fig. S9). Motors with $k_m^{\text{end}} = k_m^{\text{off}}$ exhibit an additional spike of their distribution at $\theta = \pi$ due to barbed ends acting as local attractors, between which motors move back and forth.

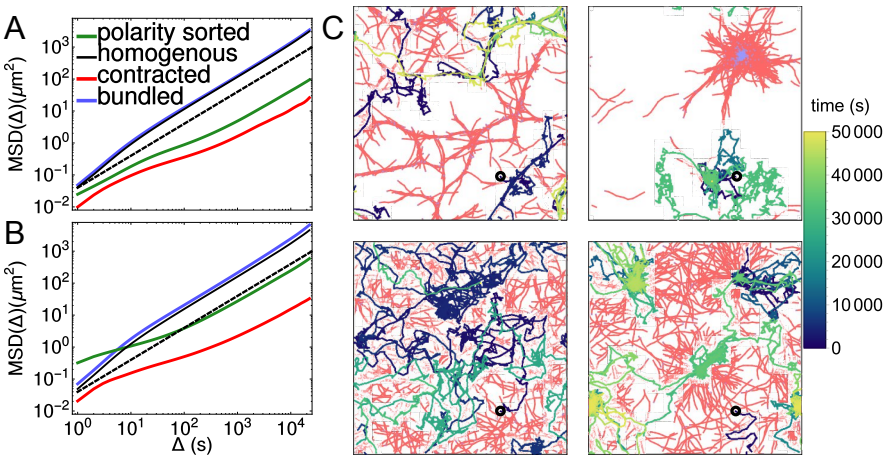

FIG. S8. Diffusion of motors on structures. Mean squared displacement of motors with $k_m^{\text{end}} = k_m^{\text{off}}$ (A) and with $k_m^{\text{end}} = 100k_m^{\text{off}}$ (B) on different actin structures. The dashed black line represents diffusion and has a slope of 1. (C) Example trajectories of motors with $k_m^{\text{end}} = 100k_m^{\text{off}}$ on the highlighted structures in Fig. 1. The initial position of each motor is shown as a black circle.

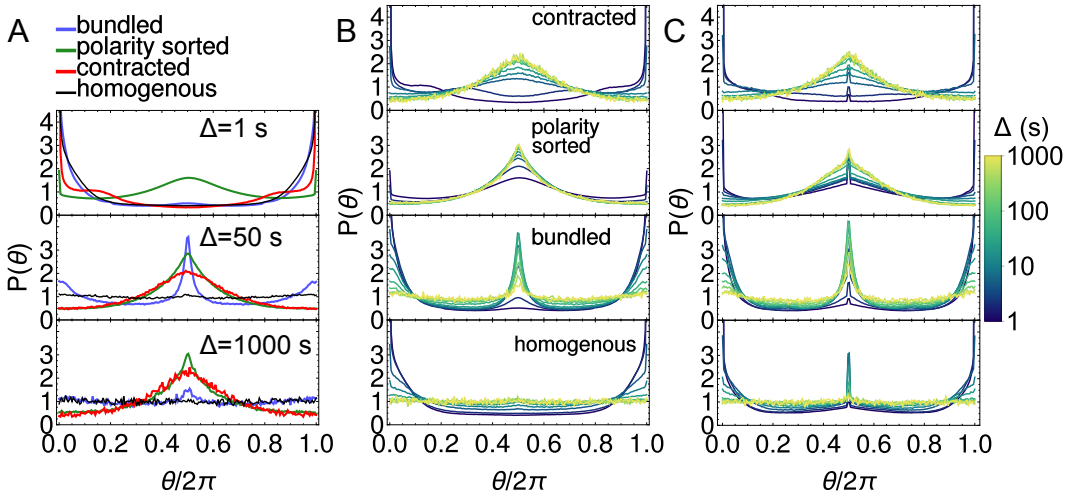

FIG. S9. Caging of motors, measured using the distribution of angles between velocity vectors [S11]. (A) Same as Fig. 5A, but for motors with $k_m^{\text{end}} = 100k_m^{\text{off}}$. (B) Caging at all time scales for all structures for motors with $k_m^{\text{end}} = 100k_m^{\text{off}}$. (C) Same as (B) but for motors with $k_m^{\text{end}} = k_m^{\text{off}}$.

S8. SIMULATING SHEAR

To measure the stiffness of self-assembled actin networks, we simulate a controlled strain experiment and shear the final network configuration by a total strain of $\gamma = 0.5$ in a fixed amount of time $t_F = 0.5$ s. This is accomplished by supplementing the Brownian Dynamics described in Section S1 by explicitly shifting the actin bead position (x_i, y_i) such that $x_i \to x_i + \gamma(dt/t_F)(y_i/Y)$ where Y is the simulation cell height, and dt is the amount of time for a small shear [S12]. Additionally, the boundary conditions follow the Lees-Edwards convention during the shear [S13]. As described in [S9], we do not perform this shift at every time step; rather $dt = \Delta t + t_{relax}$ where Δt is the simulation time step and t_{relax} is a suitable amount of time for the simulation to relax from the large external force imposed by the shear. In Fig. 2F, we used $\Delta t = 10^{-7}$ s and $dt = 10^{-3}$ s.

[S1] Benedict Leimkuhler and Charles Matthews. Robust and efficient configurational molecular sampling via langevin dynamics. *J. Chem. Phys.*, 138(17):174102, 2013.

[S2] Theo Odijk. The statistics and dynamics of confined or entangled stiff polymers. *Macromolecules*, 16(8):1340–1344, 1983.

[S3] A. Ott, M. Magnasco, A. Simon, and A. Libchaber. Measurement of the persistence length of polymerized actin using fluorescence microscopy. *Phys. Rev. E*, 48:R1642–R1645, Sep 1993.

[S4] Richard Niederman and Thomas D. Pollard. Human platelet myosin ii in vitro assembly and structure of myosin filaments. *J. Cell Biol.*, 67(1):72–92, 1975.

[S5] Stephen J. Kron and James A. Spudich. Fluorescent actin filaments move on myosin fixed to a glass surface. *Proc. Natl. Acad. Sci. USA*, 83(17):6272–6276, 1986.

[S6] Claudia Veigel, Justin E. Molloy, Stephan Schmitz, and John Kendrick-Jones. Load-dependent kinetics of force production by smooth muscle myosin measured with optical tweezers. *Nat. Cell Biol.*, 5(11):980–986, 2003.

[S7] Jorge M. Ferrer, Hyungsuk Lee, Jiong Chen, Benjamin Pelz, Fumihiko Nakamura, Roger D. Kamm, and Matthew J. Lang. Measuring molecular rupture forces between single actin filaments and actin-binding proteins. *Proc. Natl. Acad. Sci. USA*, 105(27):9221–9226, 2008.

[S8] Robert Hetland and John Travers. SciPy: Open source scientific tools for Python: rbf - radial basis functions for interpolation/smoothing scattered nd data, 2001.

[S9] Simon L Freedman, Shiladitya Banerjee, Glen M Hocky, and Aaron R Dinner. A versatile framework for simulating the dynamic mechanical structure of cytoskeletal networks. *Biophys. J*, 113(2):448–460, 2017.

[S10] Samantha Stam, Simon L. Freedman, Shiladitya Banerjee, Kimberly L. Weirich, Aaron R. Dinner, and Margaret L. Gardel. Filament rigidity and connectivity tune the deformation modes of active biopolymer networks. *Proc. Natl. Acad. Sci. U.S.A*, 114(47):E10037–10045, 2017.

[S11] Stanislav Burov, S.M. Ali Tabei, Toan Huynh, Michael P. Murrell, Louis H. Philipson, Stuart A. Rice, Margaret L. Gardel, Norbert F. Scherer, and Aaron R. Dinner. Distribution of directional change as a signature of complex dynamics. *Proc. Natl. Acad. Sci. USA*, 110(49):19689–19694, 2013.

[S12] Denis J. Evans and G. P. Morriss. Nonlinear-response theory for steady planar couette flow. *Phys. Rev. A*, 30:1528–1530, Sep 1984.

[S13] A.W. Lees and S.F. Edwards. The computer study of transport processes under extreme conditions. *J. Phys. C: Solid State Phys.*, 5(15):1921, 1972.